INTERNATIONAL JOURNAL FOR NUMERICAL METHODS IN FLUIDS
Int. J. Numer. Meth. Fluids 2002; **38**:1045–1068 (DOI: 10.1002/fld.258)

A σ-coordinate three-dimensional numerical model for surface wave propagation

Pengzhi Lin[1] and C. W. Li[2,*,†]

[1] *Department of Civil Engineering, National University of Singapore, Singapore*
[2] *Department of Civil and Structural Engineering, The Hong Kong Polytechnic University, Hong Kong*

SUMMARY

A three-dimensional numerical model based on the full Navier–Stokes equations (NSE) in σ-coordinate is developed in this study. The σ-coordinate transformation is first introduced to map the irregular physical domain with the wavy free surface and uneven bottom to the regular computational domain with the shape of a rectangular prism. Using the chain rule of partial differentiation, a new set of governing equations is derived in the σ-coordinate from the original NSE defined in the Cartesian coordinate. The operator splitting method (Li and Yu, *Int. J. Num. Meth. Fluids* 1996; **23**:485–501), which splits the solution procedure into the advection, diffusion, and propagation steps, is used to solve the modified NSE. The model is first tested for mass and energy conservation as well as mesh convergence by using an example of water sloshing in a confined tank. Excellent agreements between numerical results and analytical solutions are obtained. The model is then used to simulate two- and three-dimensional solitary waves propagating in constant depth. Very good agreements between numerical results and analytical solutions are obtained for both free surface displacements and velocities. Finally, a more realistic case of periodic wave train passing through a submerged breakwater is simulated. Comparisons between numerical results and experimental data are promising. The model is proven to be an accurate tool for consequent studies of wave-structure interaction. Copyright © 2002 John Wiley & Sons, Ltd.

KEY WORDS: σ-coordinate transformation; three-dimensional model; surface wave

INTRODUCTION

The numerical studies of surface wave propagation on uneven bottoms can be tracked back in 1960s using wave ray-tracing method [1]. As the computational power advanced since then, a few new approaches of modeling surface waves were developed and became more popular. One of them was based on the depth-averaged equations, such as shallow water equation model or Boussinesq equation model [2, 3]. The depth-averaged models are computationally efficient with the tradeoff of losing depth-related information. Another approach is based on the potential flow theory. Assuming the flow is irrotational, the velocity potential ϕ exists and the governing equation for ϕ is the Laplace equation. The numerical model that uses

---

[*] Correspondece to: C. W. Li, Department of Civil and Structural Engineering, The Hong Kong Polytechnic University, Kowloon, Hung Hom, Hong Kong SAR, People's Republic of China.
[†] E-mail: cecwli@polyu.edu.hk

Received January 2000
Revised January 2001

the boundary element method (BEM) has been developed to solve this type of flow and it has been applied to solve wave propagation problems [4]. In general, the BEM model is also computational efficient. However, it cannot be used to deal with the flows involving vortex or turbulence generation.

To solve a realistic three-dimensional problem, a numerical model with the capability of handling vorticity and even turbulence is necessary. One approach of this kind is to solve the Navier–Stokes equations (NSE) with the hydrostatic pressure assumption. This type of model is usually referred to as the quasi-three-dimensional model, which can provide three-dimensional flow patterns with affordable computational expenses. Johns and Jefferson [5] were the early explorers of this approach, though their model was only two-dimensional. Casulli and Cheng [6] presented a three-dimensional model of this type. The model was used to simulate the flooding and drying of tidal waves. This type of model can also be applied to study various turbulent channel flows [7]. Because of the employment of hydrostatic pressure assumption, such models are generally applied to shallow water flows. When the vertical acceleration of fluids is strong, i.e., wave impact on structures, the models may fail to provide accurate results.

In order to account for the effect of vertical acceleration of fluids, the full NSE must be solved. The earliest model of this kind was developed by Harlow and Welch [8] by using the Marker-and-Cell (MAC) method. However, due to the exhausting computational time, the practical three-dimensional model of this type did not become popular until the 1990s when computing powers increase significantly. For example, Thomas and Leslie [9] proposed a three-dimensional model based on the control volume technique. The model was used to study a two-dimensional inviscid large amplitude wave with periodic boundary. The model was further extended by Shi *et al.* [10] to calculate open channel flows using the Large Eddy Simulation (LES) model. Independently, Casulli [11] extended his earlier work [6] to a truly three-dimensional model. The new model was found to be more accurate than the earlier quasi-three-dimensional model when a wave train passing a submerged breakwater was studied.

In the above models, the Cartesian coordinate was used and thus the free surface normally crosses the computational cell arbitrarily. This brings the difficulty of applying the pressure boundary condition precisely on the free surface and may eventually affect the accuracy of velocity computation nearby. To solve this problem, the σ-coordinate could be introduced instead, provided that the free surface displacement is the single function of the horizontal plane. By doing so, a three-dimensional free surface flow can be mapped into a rectangular prism with the free surface being always located on the upper computational boundary. As a result, with the use of the same number of computational cells, one may obtain more accurate results by using σ-coordinate models.

Although there have been many σ-coordinate numerical models for simulating surface waves [5, 12, 13], all of the above-mentioned papers assumed hydrostatic pressure and thus they are not the fully three-dimensional models. Only until very recently, Stansby and Zhou [14] proposed a two-dimensional σ-coordinate numerical model that considered non-hydrostatic pressure. Based on their study, the inclusion of non-hydrostatic pressure in the computation is essential to accurately predict flow separations behind a steep slope. On the other hand, Hodges and Street [15] proposed another fully three-dimensional model for free surface flows using boundary fitted coordinate. Attempting to minimize the grid skewness, the Poisson grid generation method was used instead of the σ-coordinate transformation to create boundaryorthogonal grids. Such mesh generation method requires the solution of Poisson equation at each time step for the mesh generation and thus is computational demanding.

In this study, a model that solves the fully three-dimensional NSE in the σ-coordinate is proposed. Retaining the advantage of using boundary fitted coordinates, the model is computationally more economical than the Poisson grid generation method [15]. The proposed model can be used to simulate non-breaking waves propagating on uneven bottoms or wave passing through surface-piercing structures. In the following sections, governing equations and boundary conditions in the transformed plane are first presented. Numerical approximations are given next. A series of numerical tests, which include water sloshing in a confined container, solitary wave propagating in constant water depth, and periodic wave train passing a submerged breakwater, are performed to validate the proposed model. Numerical results are compared to available analytical solutions and experimental data in terms of free surface profiles and velocities.

GOVERNING EQUATIONS

Governing equations and boundary conditions in Cartesian coordinate

In the physical domain of a water wave problem, the Cartesian coordinate (x_1^*, x_2^*, x_3^*), where $x_1^* = x^*$, $x_2^* = y^*$, and $x_3^* = z^*$, with the time frame t^* are introduced. The horizontal plane is represented by (x_1^*, x_2^*). The vertical coordinate is represented by x_3^* with its origin located on the elevation of still water level. Therefore, for a non-breaking wave problem where the free surface displacement η is the single function of the horizontal plane (x_1^*, x_2^*), the physical domain in general has an irregular shape with x_3^* spanning from the bottom $-h$ to free surface η. The corresponding Navier–Stokes equations (NSE) are:

$$\frac{\partial u_I}{\partial x_I^*} = 0 \tag{1}$$

$$\frac{\partial u_I}{\partial t^*} + u_J \frac{\partial u_I}{\partial x_J^*} = -\frac{1}{\rho}\frac{\partial p}{\partial x_I^*} + g_I + \frac{\partial \tau_{IJ}}{\partial x_J^*} \tag{2}$$

where $I, J = 1, 2, 3$, u_I the velocity component in the Ith direction, p the pressure, ρ the density, and $\tau_{IJ} = v(\partial u_I/\partial x_J^* + \partial u_J/\partial x_I^*)$ the viscous stress with v the kinematic molecular viscosity.

The governing equation for the free surface displacement can be derived from the vertical integration of the continuity Equation (1) plus the appropriate boundary conditions,

$$\frac{\partial \eta}{\partial t^*} + \frac{\partial}{\partial x_J^*}\int_{-h}^{\eta} u_J \, \mathrm{d}z^* = 0 \tag{3}$$

where $J = 1, 2$.

Besides the above governing equations, different types of boundary conditions are also needed. On the bottom, the no-slip boundary condition ensures that,

$$u_I = 0 \tag{4}$$

where $I = 1, 2, 3$ and the pressure gradient in the normal direction can be derived from Equation (2) as,

$$\frac{\partial p}{\partial n^*} = \rho g_n \tag{5}$$

On the free surface, the specified pressure, which is usually taken as zero, is given,

$$p = 0 \tag{6}$$

and the continuity of tangential and normal stresses across the free surface is also enforced,

$$(\tau_{tn})_{\mathrm{water}} = (\tau_{tn})_{\mathrm{air}}; \qquad (\tau_{nn})_{\mathrm{water}} = (\tau_{nn})_{\mathrm{air}} \tag{7}$$

In the above equation, t represents the tangential direction on the free surface and n the normal direction. In the absence of wind effect, both $(\tau_{tn})_{\mathrm{air}}$ and $(\tau_{nn})_{\mathrm{air}}$ can be set to zero.

At the inflow boundary, both the free surface displacement and velocities at different elevations are specified based on either the analytical solution or the laboratory measurement of incoming flows. At the outgoing boundary, the radiation boundary condition is used to allow the flow to go out freely without reflection,

$$\frac{\partial C}{\partial t^*} + c_I \frac{\partial C}{\partial x_I^*} = 0 \tag{8}$$

where $I = 1, 2$, c_I is the wave celerity, and C could represent both η and u_J $(J = 1, 2, 3)$. Based on Equation (2), the horizontal pressure gradient at the inflow and radiation boundaries is represented by,

$$\frac{\partial p}{\partial x_I^*} = -\rho \frac{\partial u_I}{\partial t^*} - \rho u_J \frac{\partial u_I}{\partial x_J^*} + \rho g_I + \rho \frac{\partial \tau_{IJ}}{\partial x_J^*} \tag{9}$$

where again $I = 1, 2$, and $J = 1, 2, 3$.

On a vertical wall that is either within or at the boundary of the computational domain, the no-slip boundary condition as described in Equation (4) still applies. The normal gradients of pressure and free surface displacement are specified as follows,

$$\frac{\partial p}{\partial n^*} = \rho g_n \qquad \frac{\partial \eta}{\partial n^*} = 0 \tag{10}$$

where n is the normal direction to the surface of the vertical wall.

Governing equations and boundary conditions in σ-coordinate

In this study, assuming the free surface is the single function of the horizontal plane, a slightly modified σ-coordinate from Blumberg and Mellor [12] is introduced as follows,

$$t = t^* \qquad x = x^* \qquad y = y^* \qquad \sigma = \frac{z^* + h}{D} \tag{11}$$

where $D = \eta + h$. The above coordinate transformation basically maps the varying vertical coordinate in the physical domain to a uniform transformed space where σ spans from 0 to 1. The transformation process is illustrated in Figure 1. For simplicity, only x–z (x–σ) plane is shown and the y–z (y–σ) plane is defined in the same way.

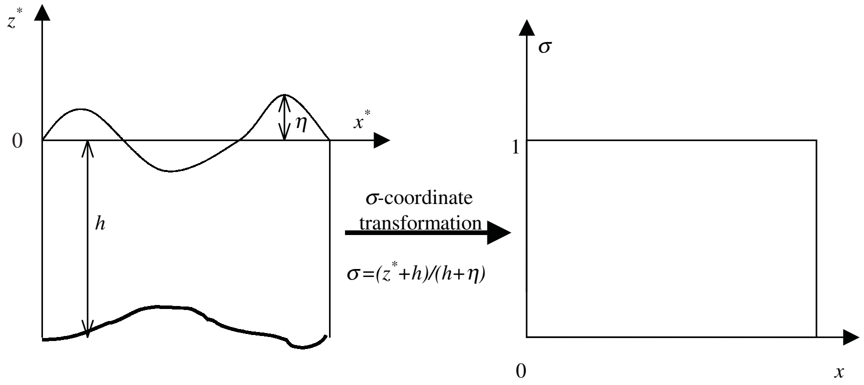

Figure 1. Illustration of σ-coordinate transformation.

Based on the principle of chain differentiation, the partial differentiation of a variable $f = f(x^*, y^*, z^*, t^*)$ in the physical domain should be modified in the transformed domain based the following rules,

$$\begin{aligned}\frac{\partial f}{\partial t^*} &= \frac{\partial f}{\partial t} + \frac{\partial f}{\partial \sigma}\frac{\partial \sigma}{\partial t^*}\\ \frac{\partial f}{\partial x^*} &= \frac{\partial f}{\partial x} + \frac{\partial f}{\partial \sigma}\frac{\partial \sigma}{\partial x^*}\\ \frac{\partial f}{\partial y^*} &= \frac{\partial f}{\partial y} + \frac{\partial f}{\partial \sigma}\frac{\partial \sigma}{\partial y^*}\\ \frac{\partial f}{\partial z^*} &= \frac{\partial f}{\partial \sigma}\frac{\partial \sigma}{\partial z^*}\end{aligned} \tag{12}$$

Substituting Equation (12) into Equations (1) and (2), we obtain the governing equations in the new coordinate (x, y, σ) and time t as follows,

$$\frac{\partial u}{\partial x} + \frac{\partial u}{\partial \sigma}\frac{\partial \sigma}{\partial x^*} + \frac{\partial v}{\partial y} + \frac{\partial v}{\partial \sigma}\frac{\partial \sigma}{\partial y^*} + \frac{\partial w}{\partial \sigma}\frac{\partial \sigma}{\partial z^*} = 0 \tag{13}$$

$$\begin{aligned}\frac{\partial u}{\partial t} + u\frac{\partial u}{\partial x} + v\frac{\partial u}{\partial y} + \omega\frac{\partial u}{\partial \sigma} = -\frac{1}{\rho}\left(\frac{\partial p}{\partial x} + \frac{\partial p}{\partial \sigma}\frac{\partial \sigma}{\partial x^*}\right) + g_x\\ + \frac{\partial \tau_{xx}}{\partial x} + \frac{\partial \tau_{xx}}{\partial \sigma}\frac{\partial \sigma}{\partial x^*} + \frac{\partial \tau_{xy}}{\partial y} + \frac{\partial \tau_{xy}}{\partial \sigma}\frac{\partial \sigma}{\partial y^*} + \frac{\partial \tau_{xz}}{\partial \sigma}\frac{\partial \sigma}{\partial z^*}\end{aligned} \tag{14}$$

$$\begin{aligned}\frac{\partial v}{\partial t} + u\frac{\partial v}{\partial x} + v\frac{\partial v}{\partial y} + \omega\frac{\partial v}{\partial \sigma} = -\frac{1}{\rho}\left(\frac{\partial p}{\partial y} + \frac{\partial p}{\partial \sigma}\frac{\partial \sigma}{\partial y^*}\right) + g_y\\ + \frac{\partial \tau_{yx}}{\partial x} + \frac{\partial \tau_{yx}}{\partial \sigma}\frac{\partial \sigma}{\partial x^*} + \frac{\partial \tau_{yy}}{\partial y} + \frac{\partial \tau_{yy}}{\partial \sigma}\frac{\partial \sigma}{\partial y^*} + \frac{\partial \tau_{yz}}{\partial \sigma}\frac{\partial \sigma}{\partial z^*}\end{aligned} \tag{15}$$

$$\frac{\partial w}{\partial t}+u\frac{\partial w}{\partial x}+v\frac{\partial w}{\partial y}+\omega\frac{\partial w}{\partial \sigma}=-\frac{1}{\rho}\frac{\partial p}{\partial \sigma}\frac{\partial \sigma}{\partial z^*}+g_z$$
$$+\frac{\partial \tau_{zx}}{\partial x}+\frac{\partial \tau_{zx}}{\partial \sigma}\frac{\partial \sigma}{\partial x^*}+\frac{\partial \tau_{zy}}{\partial y}+\frac{\partial \tau_{zy}}{\partial \sigma}\frac{\partial \sigma}{\partial y^*}+\frac{\partial \tau_{zz}}{\partial \sigma}\frac{\partial \sigma}{\partial z^*} \qquad (16)$$

where,

$$\omega=\frac{D\sigma}{Dt^*}=\frac{\partial \sigma}{\partial t^*}+u\frac{\partial \sigma}{\partial x^*}+v\frac{\partial \sigma}{\partial y^*}+w\frac{\partial \sigma}{\partial z^*} \qquad (17)$$

and,

$$\begin{aligned}\frac{\partial \sigma}{\partial t^*}&=-\frac{\sigma}{D}\frac{\partial D}{\partial t}\\ \frac{\partial \sigma}{\partial x^*}&=\frac{1}{D}\frac{\partial h}{\partial x}-\frac{\sigma}{D}\frac{\partial D}{\partial x}\\ \frac{\partial \sigma}{\partial y^*}&=\frac{1}{D}\frac{\partial h}{\partial y}-\frac{\sigma}{D}\frac{\partial D}{\partial y}\\ \frac{\partial \sigma}{\partial z^*}&=\frac{1}{D}\end{aligned} \qquad (18)$$

Since the governing equations in the transformed plane involve the terms of $[(\partial h)/(\partial x)]$ and $[(\partial h)/(\partial y)]$, the corresponding numerical model cannot treat the submerged structure with vertical wall where there exists the discontinuity of water depth gradient. However, if the structure is free surface piercing, the surface of the structure can be regarded as a solid wall where the boundary condition is applied rather than the solution is pursued.

In the transformed space, the stresses are calculated as follows,

$$\begin{aligned}&\tau_{xx}=2\nu\left(\frac{\partial u}{\partial x}+\frac{\partial u}{\partial \sigma}\frac{\partial \sigma}{\partial x^*}\right) \quad \tau_{xy}=\tau_{yx}=\nu\left(\frac{\partial u}{\partial y}+\frac{\partial u}{\partial \sigma}\frac{\partial \sigma}{\partial y^*}+\frac{\partial v}{\partial x}+\frac{\partial v}{\partial \sigma}\frac{\partial \sigma}{\partial x^*}\right)\\ &\tau_{xz}=\tau_{zx}=\nu\left(\frac{\partial u}{\partial \sigma}\frac{\partial \sigma}{\partial z^*}+\frac{\partial w}{\partial x}+\frac{\partial w}{\partial \sigma}\frac{\partial \sigma}{\partial x^*}\right) \quad \tau_{yy}=2\nu\left(\frac{\partial v}{\partial y}+\frac{\partial v}{\partial \sigma}\frac{\partial \sigma}{\partial y^*}\right)\\ &\tau_{yz}=\tau_{zy}=\nu\left(\frac{\partial v}{\partial \sigma}\frac{\partial \sigma}{\partial z^*}+\frac{\partial w}{\partial y}+\frac{\partial w}{\partial \sigma}\frac{\partial \sigma}{\partial y^*}\right) \quad \tau_{zz}=2\nu\left(\frac{\partial w}{\partial \sigma}\frac{\partial \sigma}{\partial z^*}\right)\end{aligned} \qquad (19)$$

The governing equation (3) for the free surface movement is converted into,

$$\frac{\partial \eta}{\partial t}+\frac{\partial}{\partial x}\left[D\int_0^1 u\,\mathrm{d}\sigma\right]+\frac{\partial}{\partial y}\left[D\int_0^1 v\,\mathrm{d}\sigma\right]=0 \qquad (20)$$

All the Dirichlet type of boundary conditions that give the values of the variables will remain the same. However, for the Neumann type of boundary condition that involves partial differentiation, modifications are needed in the transformed plane. For example, in the σ-coordinate, the boundary condition for pressure on bottom (Equation (5)) is changed to,

$$\frac{\partial p}{\partial \sigma} = \rho D g_z \tag{21}$$

The pressure gradient at the inflow and radiation boundaries and on the vertical wall should also be modified so that $[(\partial p)/(\partial x^*)] = [(\partial p)/(\partial x)] + [(\partial p)/(\partial \sigma)][(\partial \sigma)/(\partial x^*)]$ and $[(\partial p)/(\partial y^*)] = [(\partial p)/(\partial y)] + [(\partial p)/(\partial \sigma)][(\partial \sigma)/(\partial y^*)]$. The radiation boundary condition of Equation (8) in the transformed domain is changed to,

$$\frac{\partial C}{\partial t} + \frac{\partial C}{\partial \sigma}\frac{\partial \sigma}{\partial t^*} + c_x\frac{\partial C}{\partial x} + c_x\frac{\partial C}{\partial \sigma}\frac{\partial \sigma}{\partial x^*} + c_y\frac{\partial C}{\partial y} + c_y\frac{\partial C}{\partial \sigma}\frac{\partial \sigma}{\partial y^*} = 0 \tag{22}$$

NUMERICAL APPROXIMATIONS

In this section, the finite difference solutions to the governing equations and boundary conditions in the transformed domain are presented. Certain approximations that are employed to simplify the computation are discussed. First of all, let us define precisely the computational domain that is used in the numerical calculation. As mentioned in the previous section, the irregular physical domain with wavy free surfaces and uneven bottoms will be mapped into a regular domain with the shape of rectangular prism. This rectangular prism is then discretized by small cubes in the total number of $M \times N \times L$. All variables are defined at the corner (node) of the computational cube. They are numbered from left to right as $i = 1, 2, \ldots, M+1$ in the x-direction, $j = 1, 2, \ldots, N+1$ in the y-direction, and $k = 1, 2, \ldots, L+1$ in the σ-direction. The distance between node i and $i+1$ in the x-direction, which is also the length of the ith cube in the x-direction, is defined as Δx_i. In the same way, Δy_j and $\Delta \sigma_k$ can be defined. This is illustrated in Figure 2. In order to have the flexibility of treating the flow that has multiple length scales, non-uniform mesh system is allowed in this model, which means that it is possible $\Delta x_i \neq \Delta x_{i+1}$. All finite difference schemes given below are based on the non-uniform mesh system.

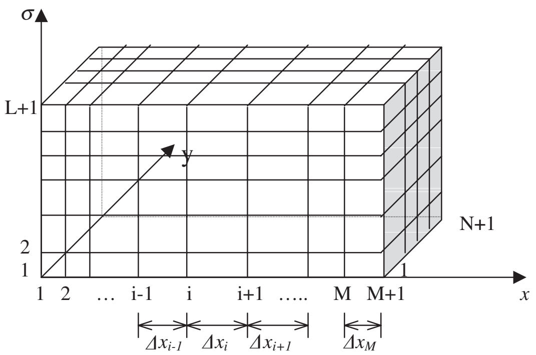

Figure 2. Schematic plot of mesh definition in σ-coordinate.

Advection step

As mentioned before, the entire computational procedure is broken into three major steps. The first step is to treat the advection terms in the momentum Equations (14) to (16). Because of the similarity of these three equations, only Equation (14) will be discussed. The other two equations can be solved in the same way.

The finite difference form for the advection step in Equation (14) can be represented as,

$$\frac{u_{i,j,k}^{n+1/3} - u_{i,j,k}^{n}}{\Delta t} + \left(u\frac{\partial u}{\partial x} + v\frac{\partial u}{\partial y} + \omega\frac{\partial u}{\partial \sigma} \right)_{i,j,k} = 0 \tag{23}$$

In fact, the above form can be further split into three sub-steps as follows,

$$\frac{u_{i,j,k}^{n+1/9} - u_{i,j,k}^{n}}{\Delta t} + \left(u\frac{\partial u}{\partial x} \right)_{i,j,k}^{n} = 0 \tag{24}$$

$$\frac{u_{i,j,k}^{n+2/9} - u_{i,j,k}^{n+1/9}}{\Delta t} + \left(v\frac{\partial u}{\partial y} \right)_{i,j,k}^{n+1/9} = 0 \tag{25}$$

$$\frac{u_{i,j,k}^{n+3/9} - u_{i,j,k}^{n+2/9}}{\Delta t} + \left(\omega\frac{\partial u}{\partial \sigma} \right)_{i,j,k}^{n+2/9} = 0 \tag{26}$$

Since the above three advection sub-steps have almost the same characteristics, they can essentially be solved by the same numerical scheme. In this study, the combination of quadratic backward characteristic method [16] and Lax–Wendroff method is used to solve the flow advection. Without losing generality, only Equation (24) is solved here. For simplicity, only $u_{i,j,k>0}$ is considered. The negative velocity and Equations (25) and (26) could be solved similarly.

In order to employ the quadratic backward characteristics method, the advection distance Δx_a is first defined as $\Delta x_a = u_{i,j,k}^{n}\Delta t$. Equation (24) is then solved as,

$$\begin{aligned}(u_{i,j,k}^{n+1/9})_{QC} = {} & \frac{(\Delta x_{i-1} - \Delta x_a)(-\Delta x_a)}{\Delta x_{i-2}(\Delta x_{i-2} + \Delta x_{i-1})} u_{i-2,j,k}^{n} \\ & + \frac{(\Delta x_{i-2} + \Delta x_{i-1} - \Delta x_a)(-\Delta x_a)}{(\Delta x_{i-2})(-\Delta x_{i-1})} u_{i-1,j,k}^{n} \\ & + \frac{(\Delta x_{i-2} + \Delta x_{i-1} - \Delta x_a)(\Delta x_{i-1} - \Delta x_a)}{(\Delta x_{i-2} + \Delta x_{i-1})\Delta x_{i-1}} u_{i,j,k}^{n}\end{aligned} \tag{27}$$

The Lax–Wendroff method solves Equation (24) as,

$$(u_{i,j,k}^{n+1/9})_{LW} = \frac{\Delta x_a(\Delta x_i + \Delta x_a)}{\Delta x_{i-1}(\Delta x_{i-1} + \Delta x_i)} u_{i-1,j,k}^{n}$$

$$+\frac{(\Delta x_{i-1}-\Delta x_a)(-\Delta x_i-\Delta x_a)}{\Delta x_{i-1}(-\Delta x_i)}\,u^n_{i,j,k}$$

$$+\frac{(\Delta x_{i-1}-\Delta x_a)(-\Delta x_a)}{(\Delta x_{i-1}+\Delta x_i)\Delta x_i}\,u^n_{i+1,j,k} \tag{28}$$

This study uses the average of the above two methods to achieve the stable and accurate numerical results, i.e.,

$$u^{n+1/9}_{i,j,k}=\lfloor (u^{n+1/9}_{i,j,k})_{QC}+(u^{n+1/9}_{i,j,k})_{LW}\rfloor/2 \tag{29}$$

Diffusion step

The diffusion process is solved after the advection is completed. Again, without the loss of generality, we still discuss Equation (14) only,

$$\frac{u^{n+2/3}_{i,j,k}-u^{n+1/3}_{i,j,k}}{\Delta t}=\left(\frac{\partial\tau_{xx}}{\partial x}+\frac{\partial\tau_{xx}}{\partial\sigma}\frac{\partial\sigma}{\partial x^*}+\frac{\partial\tau_{xy}}{\partial y}+\frac{\partial\tau_{xy}}{\partial\sigma}\frac{\partial\sigma}{\partial y^*}+\frac{\partial\tau_{xz}}{\partial\sigma}\frac{\partial\sigma}{\partial z^*}\right)^{n+1/3}_{i,j,k} \tag{30}$$

All stress terms in the above equations can be calculated based on Equation (19). The central difference method is used to discretize all partial differentiation terms in the above equation. For example,

$$\left(\frac{\partial\tau_{xx}}{\partial x}\right)^{n+1/3}_{i,j,k}=\frac{(\tau_{xx})^{n+1/3}_{i+1/2,j,k}-(\tau_{xx})^{n+1/3}_{i-1/2,j,k}}{(\Delta x_{i-1}+\Delta x_i)/2} \tag{31}$$

where

$$\begin{aligned}(\tau_{xx})^{n+1/3}_{i+1/2,j,k}&=2v\left(\frac{u_{i+1,j,k}-u_{i,j,k}}{\Delta x_i}+\frac{u_{i+1/2,j,k+1}-u_{i+1/2,j,k-1}}{\Delta\sigma_{k-1}+\Delta\sigma_k}\left(\frac{\partial\sigma}{\partial x^*}\right)_{i+1/2,j,k}\right)^{n+1/3}\\(\tau_{xx})^{n+1/3}_{i-1/2,j,k}&=2v\left(\frac{u_{i,j,k}-u_{i-1,j,k}}{\Delta x_{i-1}}+\frac{u_{i-1/2,j,k+1}-u_{i-1/2,j,k-1}}{\Delta\sigma_{k-1}+\Delta\sigma_k}\left(\frac{\partial\sigma}{\partial x^*}\right)_{i+1/2,j,k}\right)^{n+1/3}\end{aligned} \tag{32}$$

The velocity between nodes is obtained by the linear interpolation. The derivatives of σ are calculated based on formula (18). The other stress terms in Equation (30) could be discretized similarly.

Propagation step

The propagation step solves the additional source and sink terms besides the advection and diffusion. In NSE, these terms include pressure and gravitational forces. The projection method [17] is used to calculate the pressure and velocity field so that the updated velocity field satisfies the divergence-free condition as imposed by the continuity Equation (13). The finite difference forms are written as follows,

$$\frac{u^{n+1}_{i,j,k}-u^{n+2/3}_{i,j,k}}{\Delta t}=-\frac{1}{\rho}\left(\frac{\partial p}{\partial x}+\frac{\partial p}{\partial\sigma}\frac{\partial\sigma}{\partial x^*}\right)^{n+1}_{i,j,k}+g_x \tag{33}$$

$$\frac{v_{i,j,k}^{n+1} - v_{i,j,k}^{n+2/3}}{\Delta t} = -\frac{1}{\rho}\left(\frac{\partial p}{\partial y} + \frac{\partial p}{\partial \sigma}\frac{\partial \sigma}{\partial y^*}\right)_{i,j,k}^{n+1} + g_y \tag{34}$$

$$\frac{w_{i,j,k}^{n+1} - w_{i,j,k}^{n+2/3}}{\Delta t} = -\frac{1}{\rho}\left(\frac{\partial p}{\partial \sigma}\frac{\partial \sigma}{\partial z^*}\right)_{i,j,k}^{n+1} + g_z \tag{35}$$

$$\left(\frac{\partial u}{\partial x} + \frac{\partial u}{\partial \sigma}\frac{\partial \sigma}{\partial x^*} + \frac{\partial v}{\partial y} + \frac{\partial v}{\partial \sigma}\frac{\partial \sigma}{\partial y^*} + \frac{\partial w}{\partial \sigma}\frac{\partial \sigma}{\partial z^*}\right)_{i,j,k}^{n+1} = 0 \tag{36}$$

Performing the following operation:

$$\frac{\partial(33)}{\partial x} + \frac{\partial(33)}{\partial \sigma}\frac{\partial \sigma}{\partial x^*} + \frac{\partial(34)}{\partial y} + \frac{\partial(34)}{\partial \sigma}\frac{\partial \sigma}{\partial y^*} + \frac{\partial(35)}{\partial \sigma}\frac{\partial \sigma}{\partial z^*},$$

and substituting Equation (36) into the manipulation, we obtain the modified Poisson pressure equation as follows,

$$\begin{aligned}&\left\{\frac{\partial^2 p}{\partial x^2} + \frac{\partial^2 p}{\partial y^2} + \left[\left(\frac{\partial \sigma}{\partial x^*}\right)^2 + \left(\frac{\partial \sigma}{\partial y^*}\right)^2 + \left(\frac{\partial \sigma}{\partial z^*}\right)^2\right]\frac{\partial^2 p}{\partial \sigma^2}\right.\\ &\left.+2\left(\frac{\partial \sigma}{\partial x^*}\frac{\partial^2 p}{\partial x \partial \sigma} + \frac{\partial \sigma}{\partial y^*}\frac{\partial^2 p}{\partial y \partial \sigma}\right) + \left(\frac{\partial^2 \sigma}{\partial x^* \partial x} + \frac{\partial^2 \sigma}{\partial y^* \partial y}\right)\frac{\partial p}{\partial \sigma}\right\}_{i,j,k}^{n+1}\\ &= \frac{\rho}{\Delta t}\left(\frac{\partial u}{\partial x} + \frac{\partial u}{\partial \sigma}\frac{\partial \sigma}{\partial x^*} + \frac{\partial v}{\partial y} + \frac{\partial v}{\partial \sigma}\frac{\partial \sigma}{\partial y^*} + \frac{\partial w}{\partial \sigma}\frac{\partial \sigma}{\partial z^*}\right)_{i,j,k}^{n+2/3}\end{aligned} \tag{37}$$

Compared with the conventional Poisson pressure equation, the above equation has the additional cross-differential terms and other terms resulting from the coordinate transformation. The fluid density has been assumed to be constant during the derivation. Substituting finite difference forms of all derivatives in Equation (37) for all interior nodes, we obtain a system of equations as follows:

$$Aq = b \tag{38}$$

where A is a sparse matrix with the dimension of $(\mathrm{M}+1)(\mathrm{N}+1)(\mathrm{L}+1) \times (\mathrm{M}+1)(\mathrm{N}+1)(\mathrm{L}+1)$ and q is the vector of to-be-solved pressure p^{n+1}. There are totally 19 diagonal lines in A, 12 of which arise from cross-differentiations due to σ-coordinate transformation. Matrix A is positive definite and symmetric and it contains information of mesh system, free surface and bottom geometry, and boundary conditions. Vector b contains information of sources (right hand side of Equation (37)) and boundary conditions. The system of Equation (38) can be efficiently solved by conjugate gradient method with a proper pre-conditioner. In this study, the incomplete Cholesky conjugate gradient (ICCG) method as proposed by Kershaw [18] and utilized by Lin and Liu [17] will be employed as the solver to Equation (38). The description of the solver can be found in Kershaw [18] and will not be given here.

Once the correct pressure information is found at the time step $n+1$, it is substituted into Equations (33) to (35) to find the velocity information at the new time step so that the divergence free condition of Equation (36) is satisfied at time step $n+1$.

Free surface tracking step

Finally, the free surface displacement is updated by solving Equation (20). The finite difference form looks like,

$$\frac{\eta_{i,j,k}^{n+1}-\eta_{i,j,k}^{n}}{\Delta t} = -\frac{1}{\Delta x_{i-1}+\Delta x_i}\left(\Delta x_{i-1}\frac{FX_{i+1,j,k}-FX_{i,j,k}}{\Delta x_i}+\Delta x_i\frac{FX_{i,j,k}-FX_{i-1,j,k}}{\Delta x_{i-1}}\right) - \frac{1}{\Delta y_{j-1}+\Delta y_j}\left(\Delta y_{j-1}\frac{FY_{i,j+1,k}-FY_{i,j,k}}{\Delta y_j}+\Delta y_j\frac{FY_{i,j,k}-FY_{i,j-1,k}}{\Delta y_{j-1}}\right) \quad (39)$$

where FX and FY are the momentum fluxes in the x and y-directions, which can be calculated as,

$$\begin{aligned} FX_{i,j,k} &= (h+\eta)_{i,j,k}^{n}\left[\sum_{k=1}^{l} u_{i,j,k+1/2}^{n+2/3}\Delta\sigma_k + \beta\Delta t g_z\frac{\partial\eta^n}{\partial x}\right] \\ FY_{i,j,k} &= (h+\eta)_{i,j,k}^{n}\left[\sum_{k=1}^{l} v_{i,j,k+1/2}^{n+2/3}\Delta\sigma_k + \beta\Delta t g_z\frac{\partial\eta^n}{\partial y}\right] \end{aligned} \quad (40)$$

where the second term in the bracket of Equation (40) is the artificial diffusion term that will not change the leading order solution of Equation (39) but can be used to control spurious wiggles due to numerical dispersions. This treatment is similar to the Lax–Wendroff method for nonlinear advection equations. The coefficient β is the weighting coefficient that lies between 0 and 1. When $\beta=1$, the scheme is normally too dissipative; when $\beta=0$, instability could occur locally. The numerical tests show that best results are achieved when $\beta\sim 2/3$. In the following computation, $\beta=0.65$ is used unless otherwise mentioned.

Boundary conditions

Boundary conditions are applied at the end of each computational step discussed above. In this section, the details of how to apply boundary conditions are provided. Certain approximations are made to simplify the computation.

On bottom: Based on the no-slip boundary condition, particle velocities in all directions need to be zero on the bottom. This treatment, however, is accurate only when fairly fine meshes are used to resolve the bottom boundary layer. In practical computation, the resolution of the boundary layer is generally too expensive for wave propagation problems. Alternatively, the free-slip boundary condition (e.g., $\partial u/\partial\sigma = \partial v/\partial\sigma = 0$) can be used to estimate velocity gradients at the first interior node, which will be subsequently used in the advection calculation. In the meanwhile, the log-law wall function is used to calculate the wall shear stress that will be used in the diffusion step [17]. The latter method can produce reasonable results when relatively coarse meshes are used. The free-slip boundary condition without wall function can also be applied to the case when inviscid or potential flow is simulated.

On free surface: The zero pressure condition on the free surface can be easily applied when the Poisson equation is solved. The continuity of stress condition imposes the zero shear and normal stresses on the free surface when the wind effect is absent. To simplify the computation, the mild slope of free surface is further assumed, which is consistent with the premise of non-breaking wave. The original stress boundary condition on the free surface (Equation (7)) can then by simplified as follows during the computation,

$$\frac{\partial u}{\partial \sigma}=0 \qquad \frac{\partial v}{\partial \sigma}=0 \qquad \frac{\partial w}{\partial \sigma}=0 \tag{41}$$

The second-order three-point finite difference form is used to discretize the above equation. Here only the formula for u is presented,

$$u_{i,j,l+1}=\frac{(\Delta\sigma_l+\Delta\sigma_{l-1})^2}{\Delta\sigma_{l-1}(2\Delta\sigma_l+\Delta\sigma_{l-1})}u_{i,j,l}-\frac{\Delta\sigma_l^2}{\Delta\sigma_{l-1}(2\Delta\sigma_l+\Delta\sigma_{l-1})}u_{i,j,l-1} \tag{42}$$

Inflow and radiation boundaries: As mentioned before, at the inflow boundary, the velocity and free surface displacement are specified according to analytical solutions or laboratory measurements. At the radiation boundary, the velocity and free surface is updated according to Equation (22). The forward time upwind scheme is used to discretize the equation. The direction of the wave celerity is assumed to align with the local particle movement, which can be estimated by the information of local u and v.

The pressure boundary condition is worth more discussion. Although the Neumann type of boundary condition for pressure can be derived directly from the governing equation, i.e., Equation (9), the application of such a condition is complicated. In this study, the simpler condition for pressure is used in actual calculations with the assumption of negligibly small vertical acceleration of fluids at these boundaries,

$$\frac{\partial p}{\partial x}+\frac{\partial p}{\partial \sigma}\frac{\partial \sigma}{\partial x^*}=-\rho g_z\frac{\partial \eta}{\partial x} \qquad \frac{\partial p}{\partial y}+\frac{\partial p}{\partial \sigma}\frac{\partial \sigma}{\partial y^*}=-\rho g_z\frac{\partial \eta}{\partial y} \tag{43}$$

The backward difference is used to discretize the spatial differentiation.

On vertical wall: The model can also treat the interior surface-piercing structure with vertical walls. On the wall, the condition similar to that on the bottom is used for velocity. For free surface displacement and pressure, zero gradients are applied.

Stability criterion

There are two stability criteria that have to be satisfied to make the scheme stable. One is related to the advection process that is characterized by the Courant number restriction,

$$Cr_I=\frac{U_I\Delta t}{\Delta x_I}\leqslant\alpha \tag{44}$$

where $I = 1, 2, 3$ and U_I is the bigger value of maximum particle velocity and wave celerity (when in x–y plane). The value of α is 1.0 in principle but it is often taken below 0.5 to ensure the accuracy and stability everywhere in the computational domain.

Another stability restriction is related to the diffusion process. Based on the stability analysis, the following condition should be satisfied,

$$\frac{v\Delta t}{\Delta x_I^2} \leqslant \chi \tag{45}$$

where again $I = 1, 2, 3$ and χ is normally taken as 1/6 in the computation. In most of cases we studied, the maximum allowable time step is restricted by Equation (44) rather than by Equation (45).

MODEL VALIDATIONS

Water sloshing in a confined container

In this test, water sloshing in a confined container with infinite length in the y-direction is simulated. The length of the container in the x-direction is $W = 1$ m. Thus, the problem is basically two-dimensional. The free surface of the fluid in the container has the initial slope of $S = \tan\theta = 0.02$ with the still water depth of $h = 0.2$ m. Once the fluid begins to move under gravity, there exists an infinite number of standing wave modes in the container. If we neglect the viscous and nonlinear effect, the motion of the fluid could be approximated by the linear wave theory, which gives the free surface displacement as the function of x, t, and S as follows,

$$\eta = \sum_{n=1}^{\infty} A_n \sin(k_n x)\cos(\varpi_n t) \tag{46}$$

where $k_n = (n\pi)/W$ (wave number of the nth mode) and $\varpi_n = \sqrt{[g k_n \tanh(k_n h)]}$ (frequency of the nth mode), and $A_n = SW/(n^2\pi^2)[4\sin(n\pi/2) - 2\sin(n\pi)]$ (wave amplitude of the nth mode).

In the numerical simulation, the domain is discretized by an 80×20 uniform mesh system in the x–σ plane. A constant $\Delta t = 0.0015$ s is used to carry out the computation up to 7.5 s. To simulate the inviscid linear wave, the viscosity is set to zero and the free-slip boundary condition as introduced in the previous section is used. Since the leading mode $(n = 1)$ of the standing wave has the wave period $T = 2\pi/\varpi_1 = 1.5174$ s, the entire simulation covers about five wave periods for the leading mode. In Figure 3, comparisons between numerical results and analytical solutions based on Equation (59) are presented at $t/T \sim 0.0$, 0.2, 0.4, 0.6, 0.8, 1.0, 3.0, 5.0. It is noted that the analytical curves are based on the inclusion of the first 40 modes and the further increase of n will change little of the solution. The first six frames in Figure 3 correspond to the free surface variation during one wave period for the leading mode and the last two are presented to demonstrate how longer time computation behaves. From the comparisons shown in Figure 3, the numerical results agree very well with the analytical solution during the first wave. A little larger discrepancy appears in the comparisons for the longer time computation. This might be caused by the accumulated errors in the numerical model or the neglect of nonlinear effect in analytical solutions. The overall

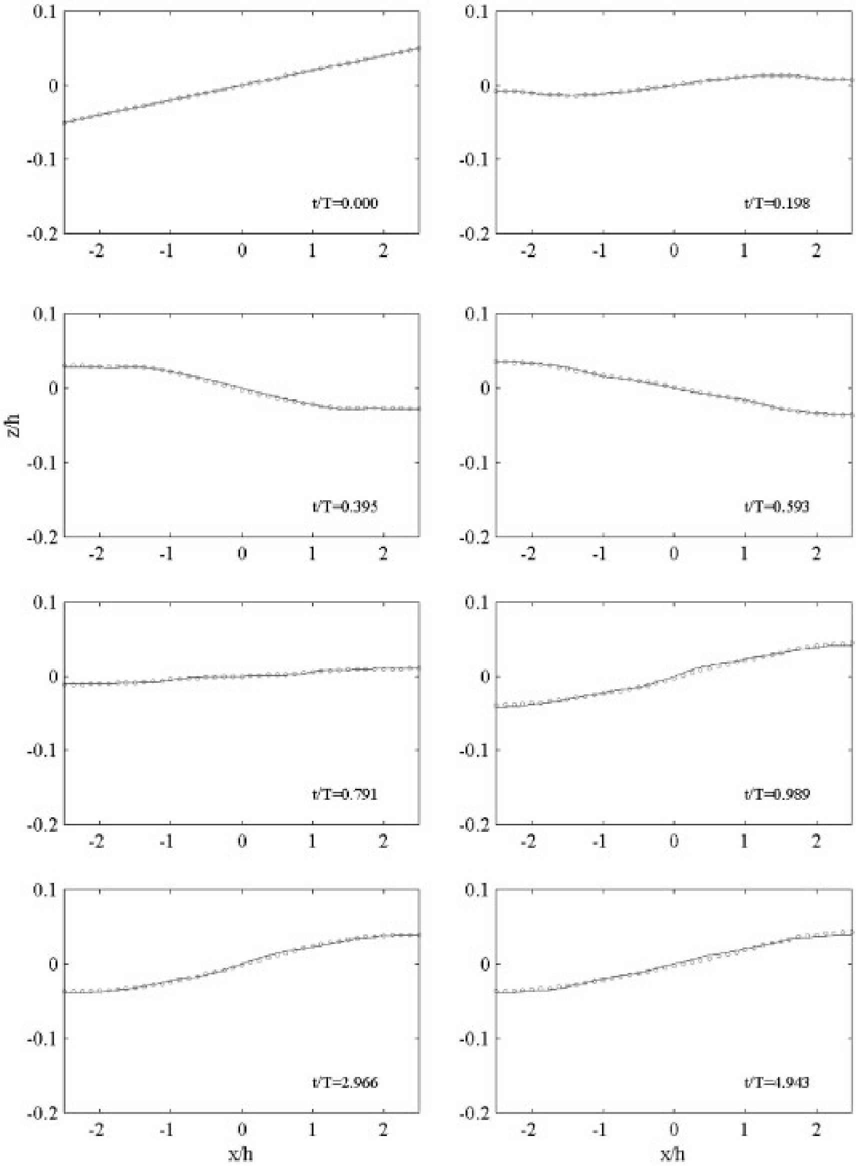

Figure 3. Comparisons of numerical results (circles) and analytical solution (solid line) for water slushing in a confined container.

comparisons, however, are fairly good, indicating that the model can predict the free surface location accurately.

The model is further tested for the conservation of total mass and energy. At $t/T = 0.0$, the total fluid mass in the tank and the associated total energy are defined as M_0 and E_0, respectively. In Figure 4, the time histories of mass M and energy (potential E_p, kinetic

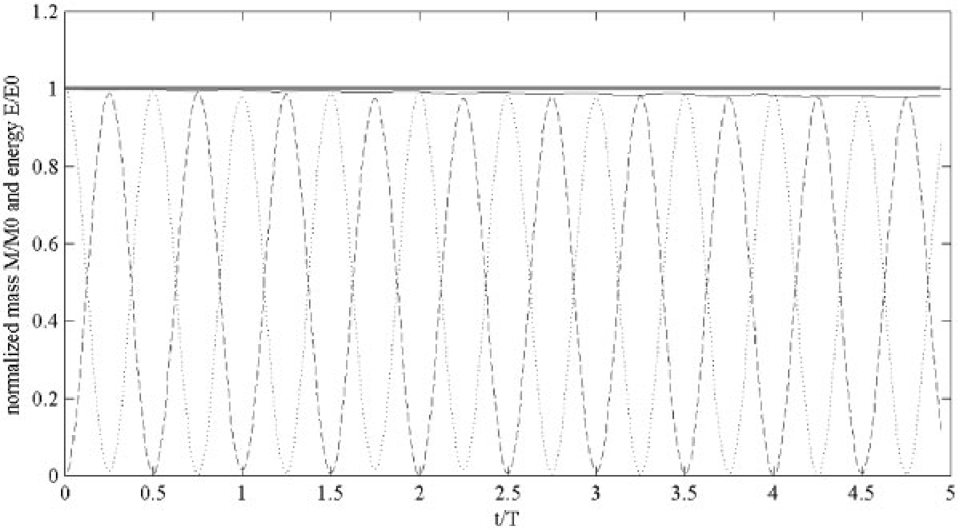

Figure 4. Calculated time histories of normalized mass (thick solid line) and total energy (solid line) = kinetic energy (dashed line) + potential energy (dotted line).

E_k, and total E_t) normalized by M_0 and E_0 are shown. It is seen that the mass is perfectly conserved within the entire computation. The potential and kinetic energy alternate during the computation with the total energy nearly conserved. The total energy decay is less than 2%, which is acceptable for most of numerical studies.

Another numerical test we have performed is to check the mesh convergence of the model, which can provide us with the useful information about the optimal mesh system for a general problem. Two additional computations using the constant mesh size and Δt half and double of those in the previous reference test are performed. The free surface displacement at $t/T \sim 3$ for these three tests are plotted together in Figure 5. The difference among three numerical results are very small, especially between the reference test and the fine mesh test, implying that the solution is already convergent in terms of free surface computation when the reference mesh system is used. Figure 6 gives the time history of the normalized total energy for three tests (mass conserves perfectly for three cases and will not be given here). It is observed that the coarse mesh system exhibits rather significant energy decay, while the fine mesh system improves the energy conservation.

The above tests imply that the criterion for mesh convergence may vary in terms of different objectives. In general, the free surface computation is less sensitive to the mesh size than the energy computation. In order to obtain the accurate results for energy, the problem should be discretized by at least the reference mesh system, i.e., about 80 meshes for a wavelength of the major mode and 20 meshes in vertical direction. However, if the free surface profile is the major concern, the coarser mesh system using about 40 grids per wavelength and 10 grids in vertical direction will be sufficient. It is also noted that the chosen problem is a very stringent test because of the existence of significant amount of high frequency modes. Thus, the good energy conservation can only be achieved by using the rather fine mesh system. Fortunately,

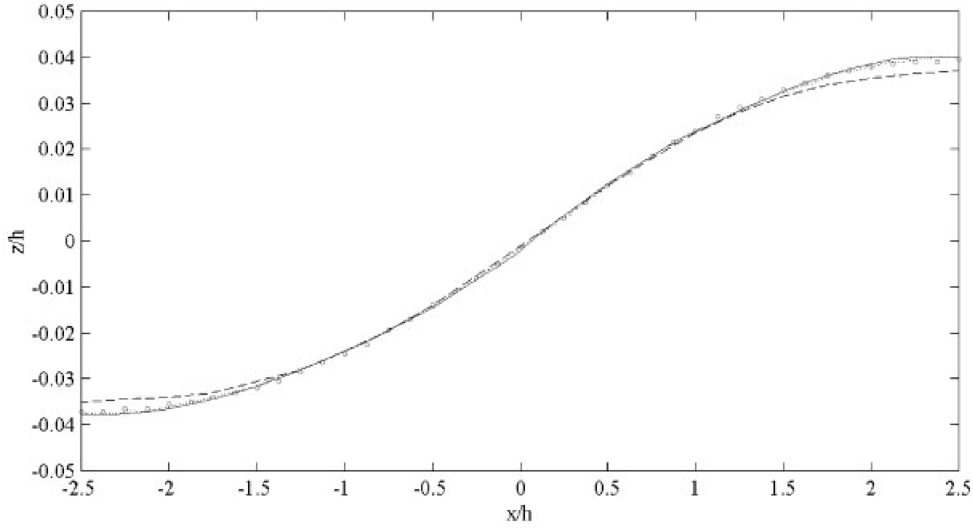

Figure 5. Convergence test in terms of free surface displacement at $t/T = 1.5$ using the reference mesh (circles), coarse mesh (dashed line), fine mesh (solid line) and non-uniform mesh (dotted line) systems.

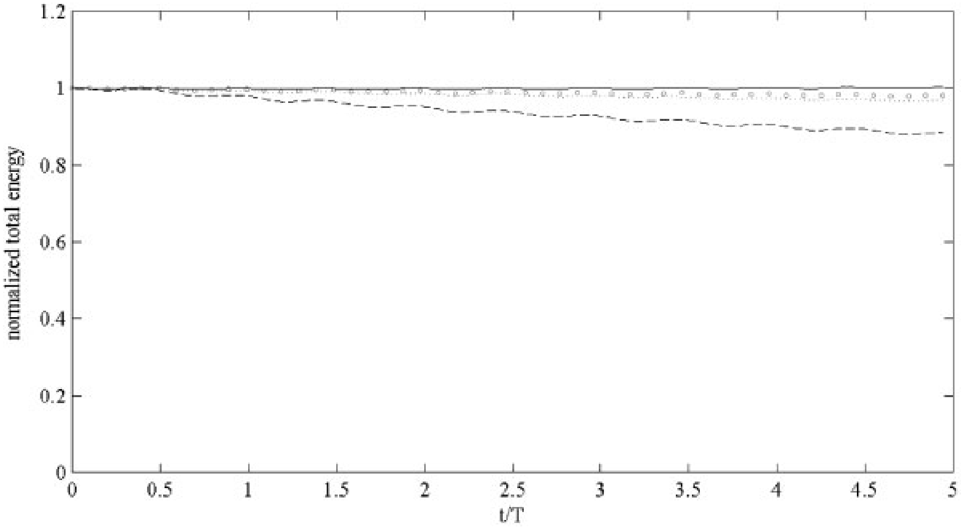

Figure 6. Convergence test in terms of energy conservation using the reference mesh (circles), coarse mesh (dashed line), fine mesh (solid line) and non-uniform mesh (dotted line) systems.

in most of other problems, the energy spectrum might be much narrower and thus a medium or even coarse mesh system would be adequate.

One more test using the non-uniform mesh system is conducted. The purpose of this test is to check the accuracy of the model when non-uniform mesh systems, which are necessary

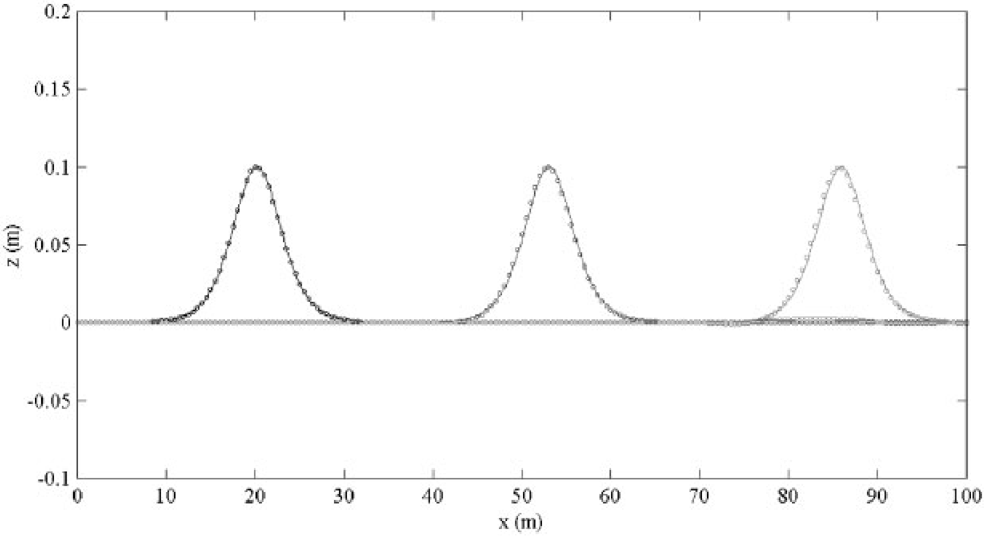

Figure 7. Comparisons of free surface displacement for a solitary wave propagation in a constant depth between numerical results (circles) and analytical solution (solid lines) at $t = 10$, 20, 30, and 40 s (from left to right).

for many practical problems, are used. The total number of mesh in this test is the same as the reference test, i.e., 80 × 20. However, finer meshes (half size of that used in the reference test) are assigned near the free surface and two sidewalls. The meshes then diverge linearly to the bottom and interior domain. This kind of deployment of meshes is often used in the computation of wave-structure interaction. In general, a non-uniform mesh system can introduce additional truncation errors and thus could have larger energy decay rate. This is confirmed in Figure 6, which shows that the total energy decays a little faster for the non-uniform mesh test. The free surface displacement, however, shows no noticeable difference from the uniform mesh results (Figure 5).

Solitary wave propagating in constant water depth In this test, a solitary wave propagating in constant water depth is simulated. The purpose of this test is to validate the inflow boundary condition for sending the proper wave and the radiation boundary condition for absorbing the outgoing wave. Both free surface profile and particle velocity are validated against analytical solutions.

First, the two-dimensional problem is investigated. A computational domain with the length in x-direction of 100 m is discretized by a uniform 1000 × 20 mesh system. The still water depth $h = 1.0$ m. A solitary wave with the wave amplitude of 0.1m is sent from the left inflow boundary by specifying the time history of free surface displacement and velocities based on the analytical solution [19]. A constant $\Delta t = 0.005$ s is used to carry out the computation up to 40 s until then the main wave train leaves the computational domain. The viscosity is again set to zero in order to compare the numerical results to the analytical solutions derived from the potential flow theory.

Figure 7 shows the comparisons between the calculated free surfaces and analytical solutions at time $t = 10$, 20, 30, and 40 s (from left to right; noted at $t = 40$ s, the main wave has

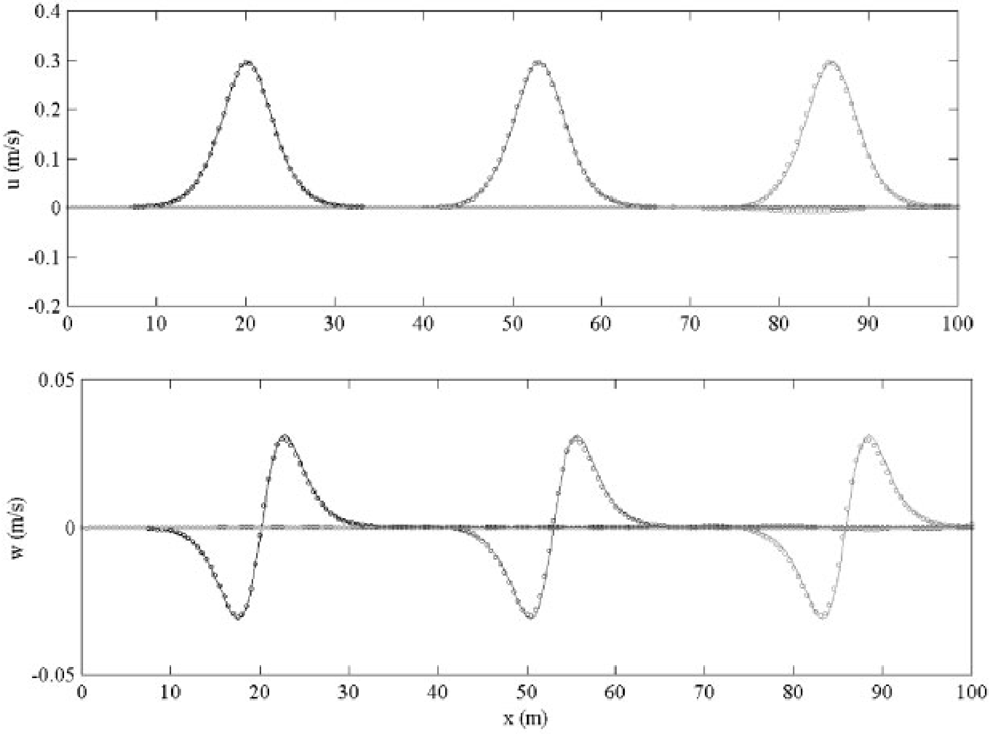

Figure 8. Comparisons of u and w at the middle elevation between numerical results (circles) and analytical solutions (solid lines).

left the domain). In the first time frame, the agreement between computation and theory is almost perfect, implying that the inflow boundary condition has behaved ideally. As time progresses, the differences in comparisons grow slightly (e.g., $t = 30$ s), indicating that either the numerical errors accumulates with time or the analytical solution degenerates for long time propagation. Nevertheless, this difference is small enough to be tolerated in the numerical modeling, considering that the wave has propagated about 100 h. The mass and energy have found to be well conserved when wave propagates in the interior domain. At $t = 40$ s, most of wave has gone out of the computational domain through the right radiation boundary. The reflection wave detected is only 2% of the incident wave in terms of wave amplitude, and about 0.05% in terms of wave energy.

Figure 8 shows the comparisons of horizontal and vertical velocities between the calculation and theory on the middle elevation of the water depth at $t = 10$, 20 and 30 s. Fair comparisons are obtained. Although most quasi-three dimensional models can provide almost the same accurate calculation for horizontal velocity, they can hardly give the accurate result for vertical velocity due to the neglect of dynamic pressure. The good agreement in Figure 8 for the vertical velocity indicates that the dynamic pressure has been well simulated by this model, which is very important when the problem of wave-structure interaction is studied.

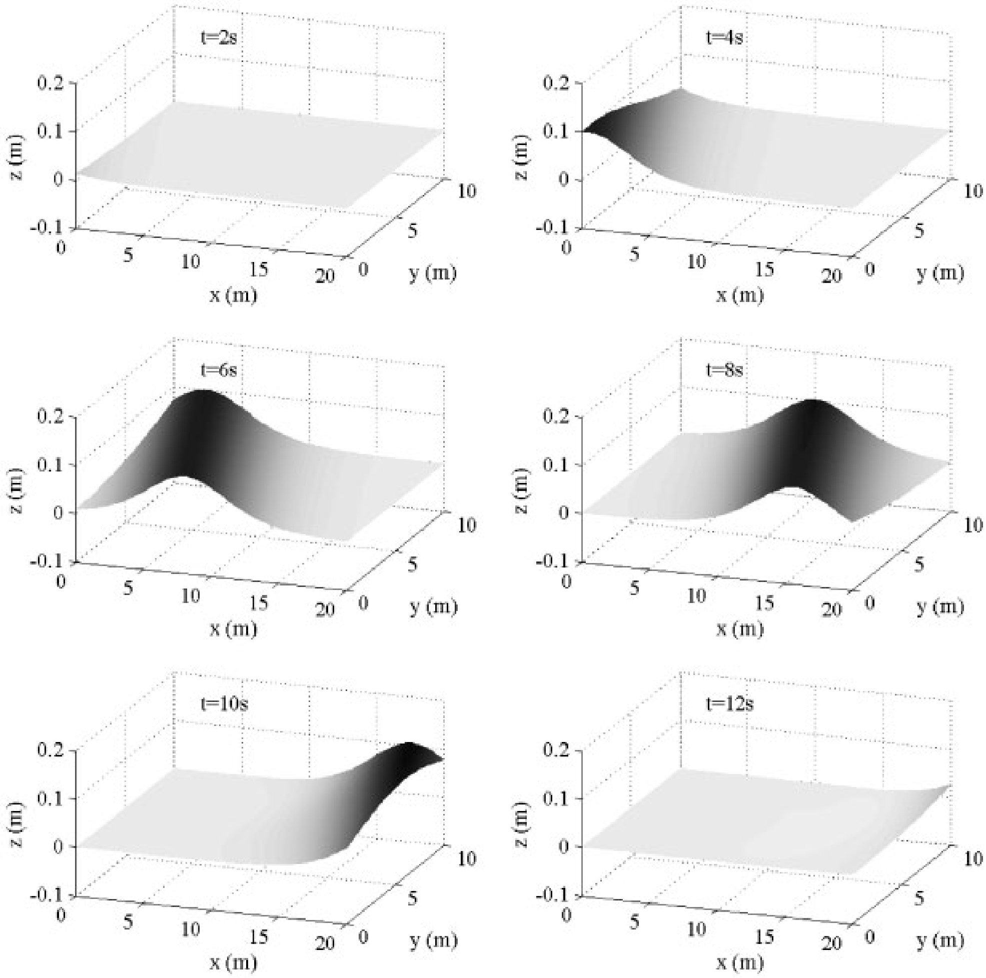

Figure 9. Surface plot of the evolution of obliquely incident solitary wave propagation in constant depth.

To test how the model behaves in a three-dimensional situation, the above problem is investigated from another point of view. In the new test, the wave train is sent from the left and front boundaries at an angle of $\theta = 30°$ (the previous case could now be regarded as the special case when $\theta = 0°$). The right and back boundaries are set to be radiation boundaries. Since the wave is sent from an oblique direction, the behavior of the model in a realistic three-dimensional problem could be simulated. A shorter computational domain with the horizontal plane of $20\,\mathrm{m} \times 10\,\mathrm{m}$ is discretized by a uniform mesh system with $200 \times 100 \times 20$ meshes. Figure 9 gives the surface plots for the evolution of the wave train at the time interval of 2 s from $t = 2$ to $t = 12$ s. It is seen that the waveform remains nearly permanent during the propagation, agreeing with the theoretical expectation. The further validation by directly comparing the free surface displacement between computation and theory at $t = 4$, 6, 8, and

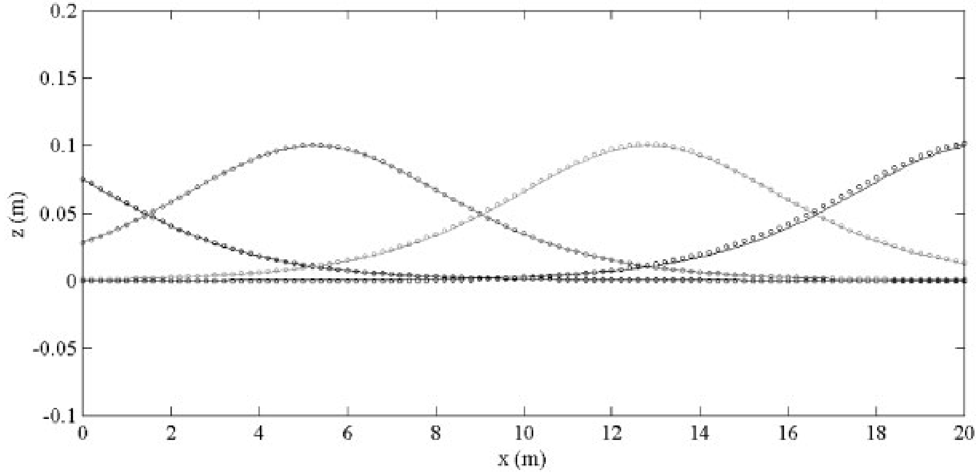

Figure 10. Comparison of free surface displacement of an obliquely incident solitary wave between numerical results (circles) and analytical solution (solid lines) at the section $y = 5$ m and $t = 4$, 6, 8, and 10 s (from left to right).

10s (see Figure 10) confirms the observation. This test demonstrates the accuracy of the model for the three-dimensional computation. The radiation boundary condition of Equation (28) for absorbing the oblique wave is also proven to be accurate.

Periodic wave train passing a submerged breakwater

Submerged breakwaters are usually deployed in the coastal area to reduce the wave energy transmission. When a wave train passes through a submerged breakwater, it normally experiences dramatic changes of waveform and significant nonlinear energy transfer among different wave modes. Flow separations can be induced if the breakwater slope is steep. Under such circumstance, the hydrostatic pressure assumption becomes invalid. Beji and Battjes [20, 21] investigated this problem experimentally and numerically. They found that very poor predictions could result if the dispersion terms, which reflect the influence of non-hydrostatic pressure, are not properly modeled in the Boussinesq equations. Casulli [11] solved the same problem numerically by using his model based on Navier–Stokes equations. He also found that by including the non-hydrostatic pressure, wave transformation was predicted very well. The hydrostatic model, however, gave totally unrealistic prediction.

In this study, we attempt to simulate a similar problem. Experiments that have almost the same setup as that in Beji and Battjes [20] but with larger scale were conducted in Delft Hydraulics (Figure 11). A regular wave train that has the wave height of 0.04 m and wave period of 2.86 s was sent from the left boundary ($x = 0$). The absorbing beach was installed on the right side of wave flume in the experiment but was replaced by a radiation boundary in constant water depth in the numerical simulation, as shown in Figure 11. Totally 10 wave gauges were deployed at $x = 3.04$ m, 9.44 m, 20.04 m, 24.04 m, 26.04 m, 28.04 m, 30.44 m, 33.64 m, 37.04 m, and 41.04 m, respectively. A two-dimensional mesh system of 1000×20 is used to discretize the entire computational domain. The time step is chosen to be $\Delta t = 0.01$ s.

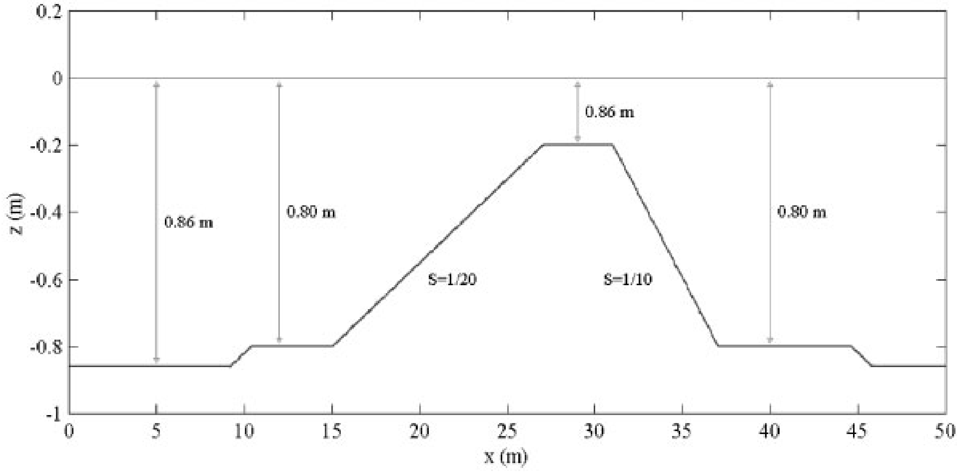

Figure 11. Experimental setup of a periodic wave train passing a submerged breakwater.

The computation is carried out up to $t = 45$ s. The viscous effect has been included in the simulation ($v = 1.0 \times 10^{-6}$) that will be discussed below. The simulation without viscosity has also been conducted for reference and it is found that the differences in terms of free surface displacement between two simulations are less than 0.1%, which implies that the viscous effect is not significant for this case.

Figure 12 shows comparisons between numerical results and gauge data for free surface displacement at the last eight wave gauge locations. At the first two gauge locations, the wave train remains sinusoidal with nearly perfect agreements between numerical results and experimental data and they are not shown in Figure 12. From $x = 20.04$ to $x = 24.04$ m where wave starts to climb the slope, the gradually increasing wave steeping due to shoaling effects is observed. At $x = 26.04$ m, 28.04 m and 30.44 m, where the wave rides over the top of breakwater, the growth of secondary wave becomes apparent. The numerical model captures this process accurately, though some details of wave signature do not completely agree between numerical results and experimental data.

Behind the breakwater, the secondary wave mode gains energy from the main wave mode and the effective wavelength becomes shorter. This can be seen at the last three gauge locations. In general, the prediction of wave transformation in this region is of the most difficulty because of the complicated flow separation and nonlinear wave energy transfer. Rigorously speaking, a proper turbulence model needs to be included to simulate this physical process correctly. Since the present model neglects the turbulence effect, the discrepancies between numerical results and experimental data become larger in this region compared with those at upstream gauge locations. Similar discrepancies, i.e., overestimation of trough level when waves re-enter into constant water depth (e.g., $x = 37.04$ m in Figure 12), have also shown in Casulli's [11] simulation (e.g., Figure 5 in his paper), which neglects the turbulence effect too. Nevertheless, the overall agreements between the numerical results and experimental data are still very encouraging. This demonstrates that the model has the capability of simulating complicated problems of wave-structure interaction, which we shall explore further for the three-dimensional case in the future [22].

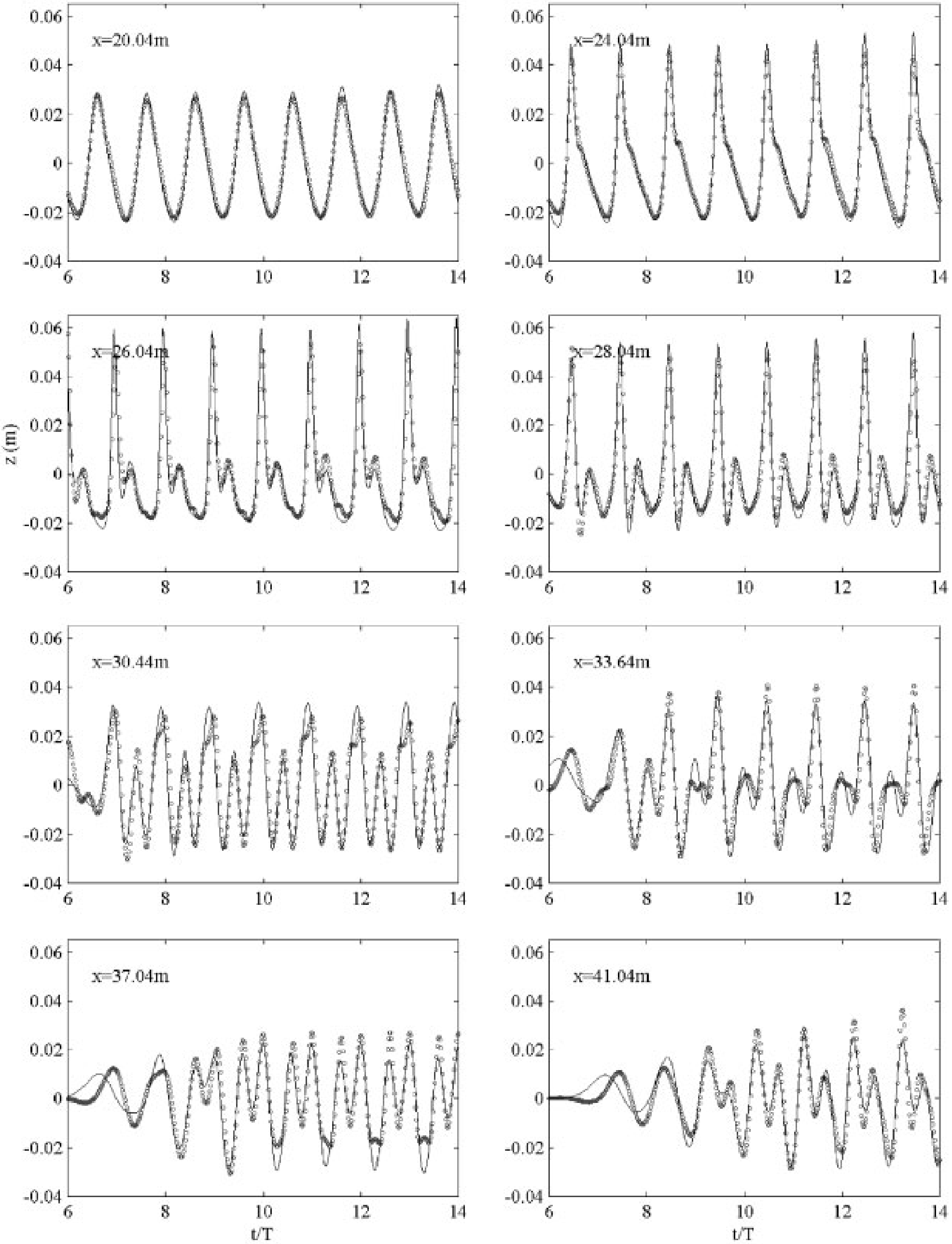

Figure 12. Comparisons of free surface displacement at the last eight wave gauge locations between numerical results (solid lines) and experimental data (circles).

CONCLUSION

In this study, a new model that solves the NSE in the three-dimensional σ-coordinate has been developed. The model retains the advantage of solving the full NSE without neglecting the dynamic pressure, which is important for calculating vertical velocities accurately. Furthermore, the employment of σ-coordinate simplifies the application of pressure boundary condition on free surfaces and thus improves the computational accuracy. The proposed model is validated by a series of numerical tests that include wave sloshing in a tank, solitary wave propagation in constant water, and periodic wave passing a submerged breakwater. The accuracy of the model for predicting the free surface displacement and velocities is excellent, provided the reasonable numerical resolution is used. The model conserves mass perfectly for all testing cases even with the use of coarse meshes. Satisfactory energy conservation, however, normally requires relatively fine mesh resolution, especially for cases where significant amount of high frequency wave modes is present. For most practical problems involving wave propagation, in order to obtain the accurate results for energy computation, a mesh system that resolves a wavelength by 80 meshes and water depth by 20 meshes is suggested. On the other hand, if the free surface information is the major objective, a coarser mesh system of 40×10 for a wavelength would be adequate. In the near future, the validated model will be applied to study the turbulent channel flow by including a LES model as proposed by Li and Wang [23]. The model will also be used to study three-dimensional wave-structure interactions.

ACKNOWLEDGEMENTS

The research work herein was supported by the postdoctoral fellowship for P. Lin from The Hong Kong Polytechnic University (G-YW28). The authors would also like to thank Dr Maarten W. Dingemans in Delft Hydraulics for providing us experimental data for the last testing case.

REFERENCES

1. Wilson WS. A method for calculating and plotting surface wave rays. Tech. Memo. 17, U.S. Army, Coastal Engineering Research Center, 1966.
2. Liu PL-F, Yoon SB, Seo SN, Cho Y-S. Numerical simulation of tsunami inundation at Hilo, Hawaii. *Recent Development in Tsunami Research* (ed. El-Sabh, M. I.). Kluwer Academic Publishers: New York, 1994.
3. Abbott MB, McCowan AD, Warren IR. Accuracy of short-wave numerical models. *Journal of Hydraulics Engineering* 1985; **110**(10):1287–1301.
4. Grilli S, Svendsen IA. Wave interaction with steeply sloping structures. Proceedings of the 22nd International Conference on Coastal Engineering, ASCE, 1990, pp. 1200–1213.
5. Johns B, Jefferson RJ. The numerical modeling of surface wave propagation in the surf zone. *Journal of Physical Oceanography* 1980; **10**:1061–1069.
6. Casulli V, Cheng RT. Semi-implicit finite difference methods for three-dimensional shallow water flow. *International Journal for Numerical Methods in Fluids* 1992; **15**:629–648.
7. Li CW, Yu TS. Numerical investigation of turbulent shallow recirculating flows by a quasi-three-dimensional *k–e* model. *International Journal for Numerical Methods in Fluids* 1996; **23**:485–501.
8. Harlow FH, Welch JE. Numerical calculation of time-dependent viscous incompressible flow. *Physics of Fluids* 1965; **8**:2182–2189.
9. Thomas TG, Leslie DC. Development of a conservative 3D free surface code. *Journal of Hydraulics Research* 1992; **30**:107–115.
10. Shi J, Thomas TG, Williams JJR. Development of a large-eddy simulation open channel code. *International Journal for Numerical Methods in Heat & Fluid Flow* 1999; **9**:6–17.
11. Casulli V. A semi-implicit finite difference method for non-hydrostatic, free-surface flows. *International Journal for Numerical Methods in Fluids* 1999; **30**:425–440.
12. Blumberg AF, Mellor GL. Diagnostic and prognostic numerical circulation studies of the South Atlantic Bight. *Journal of Geophysics Research* 1983; **88**(C8):4579–4592.

13. Burchard H, Petersen O. Hybridization between σ- and z-co-ordinates for improving the internal pressure gradient calculation in marine models with steep bottom slopes. *International Journal for Numerical Methods in Fluids* 1997; **25**:1003–1023.
14. Stansby PK, Zhou JG. Shallow-water flow solver with non-hydrostatic pressure: 2D vertical plane problems. *International Journal for Numerical Methods in Fluids* 1998; **28**:541–563.
15. Hodges BR, Street RL. On simulation of turbulent nonlinear free-surface flows. *Journal of Computational Physics* 1999; **151**:425–457.
16. Zhu L, Li CW. Error study on numerical approximation of radiation boundary condition for one-dimensional wave equation. *Communications in Numerical Methods in Engineering* 1993; **9**:475–482.
17. Lin P, Liu PL-F. A numerical study of breaking waves in the surf zone. *Journal of Fluid Mechanics* 1998; **359**:239–264.
18. Kershaw DS. The incomplete Cholesky—conjugate gradient method for the iterative solution of system of linear equations. *Journal of Computational Physics* 1978; **26**:43–65.
19. Lee, J-J, Skjelbreia E, Raichlen F. Measurement of velocities in solitary waves. *Journal of Waterway*, *Port*, *Coastal and Ocean Division* 1982; **108**(WW2):200–218.
20. Beji S, Battjes JA. Experimental investigation of wave propagation over a bar. *Coastal Engineering* 1993; **19**:151–162.
21. Beji S, Battjes JA. Numerical simulation of nonlinear wave propagation over a bar. *Coastal Engineering* 1994; **23**:1–16.
22. Li CW, Lin P. A numerical study of three-dimensional wave interaction with a square cylinder. *Ocean Engineering* 2000; accepted for publication.
23. Li CW, Wang JH. Large eddy simulation of free surface shallow water flow. *International Journal for Numerical Methods in Fluids* 2000; **34**(1):31–46.